

# The dark matter distribution in $z \sim 0.5$ clusters of galaxies

## I : Determining scaling relations with weak lensing masses <sup>★</sup>

G. Foëx<sup>1,2</sup>, G. Soucail<sup>1,2</sup>, E. Pointecouteau<sup>1,3</sup>, M. Arnaud<sup>4</sup>, M. Limousin<sup>5,6</sup>, and G.W. Pratt<sup>4</sup>

<sup>1</sup> Université de Toulouse; UPS-Observatoire Midi-Pyrénées; IRAP; Toulouse, France

<sup>2</sup> CNRS; Institut de Recherche en Astrophysique et Planétologie (IRAP); 14 Avenue Edouard Belin, F-31400 Toulouse, France

<sup>3</sup> CNRS; Institut de Recherche en Astrophysique et Planétologie (IRAP); 9 avenue Colonel Roche, F-31028 Toulouse cedex 4, France

<sup>4</sup> Laboratoire AIM; IRFU/Service d'Astrophysique; CEA/DSM; CNRS and Université Paris Diderot; Bât. 709, CEA-Saclay, F-91191 Gif-sur-Yvette Cedex, France

<sup>5</sup> Laboratoire d'Astrophysique de Marseille (LAM); Université d'Aix-Marseille & CNRS; UMR7326; 38 rue Frédéric Joliot-Curie, F-13388 Marseille Cedex 13, France

<sup>6</sup> Dark Cosmology Centre, Niels Bohr Institute, University of Copenhagen; Juliane Maries Vej 30, DK-2100 Copenhagen, Denmark

Received ; accepted

### ABSTRACT

The total mass of clusters of galaxies is a key parameter to study massive halos. It relates to numerous gravitational and baryonic processes at play in the framework of large scale structure formation, thus rendering its determination important but challenging. From a sample of the 11 X-ray bright clusters selected from the EXCPRES sample, we investigate the optical and X-ray properties of clusters with respect to their total mass derived from weak gravitational lensing. From multi-color wide field imaging obtained with MegaCam at CFHT, we derive the shear profile of each individual cluster of galaxies. We perform a careful investigation of all systematic sources related to the weak lensing mass determination. The weak lensing masses are then compared to the X-ray masses obtained from the analysis of XMM-Newton observations and assuming hydrostatic equilibrium. We find a good agreement between the two mass proxies although a few outliers with either perturbed morphology or poor quality data prevent to derive robust mass estimates. The weak lensing mass is also correlated with the optical richness and the total optical luminosity, as well as with the X-ray luminosity, to provide scaling relations within the redshift range  $0.4 < z < 0.6$ . These relations are in good agreement with previous works at lower redshifts. For the  $L_X - M$  relation we combine our sample with two other cluster and group samples from the literature, thus covering two decades in mass and X-ray luminosity, with a regular and coherent correlation between the two physical quantities.

**Key words.** Gravitational lensing: weak – X-rays: galaxies: clusters – Cosmology: observations – Cosmology: dark matter – Galaxies : clusters : general – Galaxies : clusters : individual

## 1. Introduction

Clusters of galaxies have been attracting considerable interest for their cosmological applications since a few decades. The observed cluster abundance, converted into a mass function, can be confronted to cosmological numerical simulations to put tight constraints on cosmological parameters like the amplitude of matter fluctuations or the dark energy density (Bahcall & Cen 1992; White et al. 1993; Haiman et al. 2001; Wang et al. 2004; Albrecht et al. 2006; Mandelbaum & Seljak 2007; Rozo et al. 2009). The main limitation in the use of this mass function is the practical determination of the masses themselves. In the simplest model of structure formation and evolution which involves a pure gravitational collapse of dark matter halos, groups and clusters are expected to form a population of self-similar objects characterized by simple relations linking the total mass to other physical quantities (Kaiser 1986). These scaling relations represent an efficient way to convert simple observables to masses for large samples of objects. However, the link between the to-

tal mass of an object and its baryonic tracers is not fully understood. Several processes break the self-similarity and introduce a scatter around the theoretical relation that needs to be accounted for when determining the mass function (see Voit 2005 for a review). Hydrodynamic simulations offers a way to complete this model. They can define more realistic relations between the cluster total mass and the X-ray observables (e.g. Kravtsov et al. 2006; Nagai et al. 2007). But the physics of the baryons within these simulations is not well constrained. Therefore, it is of prime importance to characterize and calibrate scaling relations with observational results based on accurate direct mass measurements. Such empirical relations can also improve our understanding of several non-gravitational processes disturbing the evolution of the large-scale structures.

Among the several ways to derive the total mass of a cluster of galaxies, an efficient one is to use the X-ray emission of the intra-cluster gas. The distribution in density and temperature can be measured and, assuming the hydrostatic equilibrium of the cluster, it is possible to derive the dark matter potential shape. This kind of approach has been applied successfully on many X-ray observations (Pointecouteau et al. 2005; Vikhlinin et al. 2006; Buote et al. 2007). However, masses derived from the X-ray measurements suffer systematics from non-relaxed objects or from non-thermal pressure support, and tends to underesti-

<sup>★</sup> Based on observations obtained with MegaPrime/MegaCam, a joint project of CFHT and CEA/DAPNIA, at the Canada-France-Hawaii Telescope (CFHT) which is operated by the National Research Council (NRC) of Canada, the Institut National des Science de l'Univers of the Centre National de la Recherche Scientifique (CNRS) of France, and the University of Hawaii.

mate the true total mass of clusters by  $\sim 10 - 15\%$  as seen in numerical simulations (Kay 2004; Nagai et al. 2007; Lau et al. 2009; Meneghetti et al. 2010) and suggested by observational results (e.g. Mahdavi et al. 2008).

Gravitational lensing is another way to derive the total projected mass, without any assumption about the dynamical state of the cluster. The strong lensing regime that occurs in the center of some clusters leads to elongated arcs and multiple images of background galaxies which probe the central mass distribution. In parallel, the weak lensing regime leads to estimates of the total mass through the statistical distortion of background galaxies up to large projected distances from the cluster center (e.g. Bartelmann & Schneider 2001 for a review). However, this method gives reliable results only for massive clusters in which the weak lensing signal is detectable with high enough accuracy. It is also limited to intermediate redshift clusters for which the distant background galaxies are far enough behind the cluster. Gravitational lensing masses are also subject to systematics such as the determination of the redshift distribution of the sources or projection effects of matter structures near the cluster or along the line-of-sight (Metzler et al. 2001; Hoekstra 2003; Meneghetti et al. 2010).

Because all these mass estimators have their own weaknesses and limits and because they fail to properly recover the total mass in specific cases, there has been attempts to provide joint analysis of the mass profiles, combining strong and weak lensing (Kneib et al. 2003; Bradač et al. 2005; Merten et al. 2009; Oguri et al. 2011) or lensing and X-ray measurements (Mahdavi et al. 2007; Morandi et al. 2010). But the difficulty to get data of similar "quality" to combine them efficiently has up to now limited the use of such analysis.

In order to better quantify the scaling relations of clusters with weak lensing masses, we present in this paper the study of a sample of 11 intermediate redshift clusters which are part of the EXCPRES sample. These clusters have been observed in X-ray with XMM-Newton (Arnaud et al. in preparation) and in wide field optical imaging with Megacam at the Canada-France-Hawaii Telescope (Foëx et al. 2012, hereafter Paper 2). The paper is organized as follows. In section 2 we present the sample of 11 clusters selected for this study. Section 3 is dedicated to the lensing methodology with special attention to the shape measurements of the background galaxies and the normalization of the lensing signal. Lensing masses are determined from the shear signal in section 4 where we also make the comparison with the X-ray masses. Scaling relations are built and discussed in section 5 and some conclusions are drawn in section 6. In all the paper, we assume a standard  $\Lambda$ -CDM cosmology with  $\Omega_M = 0.3$ ,  $\Omega_\Lambda = 0.7$  and  $H_0 = 70 h_{70} \text{ km s}^{-1} \text{ Mpc}^{-1}$ .

## 2. The cluster sample description

The 11 clusters used in the present study are a sub-sample of the EXCPRES sample (*Evolution of X-ray galaxy Cluster Properties in a REpresentative Sample*, Arnaud et al. in preparation). This is a representative X-ray selected sample of clusters in the redshift range  $0.4 < z < 0.6$ , compiled from published X-ray selected samples at the end of 2004 (e.g., EMSS, NORAS, REFLEX, B-SHARC, S-SHARC, 160SD and WARPS-I samples). EXCPRES is designed to study the evolution of the X-ray properties of clusters. Objects are selected only on the basis of their X-ray luminosities, as measured in the aforementioned surveys, and their redshift. The EXCPRES clusters are selected in the  $L_X - z$  plane around a median redshift of  $z = 0.5$ , so that there are about 5 clusters in roughly

equal logarithmically-spaced luminosity bins (factor of  $\sim 2$  variation between bins). No selection is added with respect to the dynamical state, ensuring that no bias is introduced by the sample construction process, making it ideal for the study of scaling relations and their evolution. The final sample contains 20 clusters.

The main issue to deal with such a sample of clusters is the selection bias. The 3 clusters from the surveys with a strict X-ray surface brightness limit (B-SHARC and REFLEX) are at 1-2 times the survey limit, i.e. in the regime where the bias is not negligible. For the other clusters from the EMSS and NORAS surveys, that have no defined flux limits, it is difficult to say whether there is a bias. Note however that NORAS clusters are below the  $3e^{-12}$  flux limit where the survey is 50% complete, so likely introducing a bias. Therefore, there is most likely a Malmquist bias, that in principle should be taken into account for the study of the  $L_X - M$  relation. However it is basically impossible to estimate precisely this bias due to the variety of cluster surveys from which we constructed the EXCPRES sample. Note also that both the  $L_X - M$  relations from Rykoff et al. (2008) and Leauthaud et al. (2010) (compared and combined with our results in section 5.3) are not corrected for the Malmquist bias. This issue represents a limitation for precise studies of the  $L_X - M$  scaling relation.

However for the  $M_X - M_{WL}$  mass relation, the original main goal of this paper, the Malmquist bias effect should not be important. It could play a role via possible residual bias in dynamical state: X-ray surveys preferentially select highly peaked cool core (thus relaxed) clusters close to the survey flux limit because they are over-luminous for their mass. Thus the sample may contain more relaxed clusters than the underlying population. This may affect the  $M_X - M_{WL}$  relation as one expects better agreement for relaxed objects. However in view of the error bars and dispersion (see Figure 6), this is not the major worry.

Note that EXCPRES is deliberately built in a similar way to the local representative sample REXCESS (Böhringer et al. 2007); so the scaling and structural properties of REXCESS (Croston et al. 2008; Pratt et al. 2009; Arnaud et al. 2010) will be used as a local reference for EXCPRES.

Only clusters with an X-ray luminosity  $L_X > 5 \times 10^{44} \text{ erg/s}$  in the [0.5-2.0] keV band within the detection radius were selected for an optical follow-up. This threshold in  $L_X$  ensures that the total mass of each cluster is high enough to provide significant weak lensing signal. These measured XMM-Newton luminosities were converted into the [0.1-2.4] keV energy band for further analysis and comparison with other works (see Sec. 5.3). They are reported Table 1 together with global temperatures derived within apertures maximizing the signal-to-noise ratio for the XMM-Newton spectroscopic analysis. In the framework of the EXCPRES project, the weak lensing measurement of these 11 clusters allows a one-to-one comparison of the X-ray and weak lensing mass proxies to assess the reliability of the total mass estimate from X-rays data only.

## 3. Weak lensing

Gravitational lensing distorts the intrinsic image of the background galaxies. This is usually quantified by the change in the shape parameters of the sources. But the intrinsic shape is convolved by the effect of the atmosphere and the instrumental distortion before it is measured on CCD images. The PSF correction is therefore a critical step in the weak lensing analysis and it has to be done with great care. This is usually validated thanks

**Table 1.** General properties of the clusters. Columns: (1) Cluster Name. (2,3) Equatorial coordinates of the X-ray peak. (4) Redshift. (5) X-ray luminosity in the XMM-Newton [0.1-2.4] keV energy band within the detection radius,  $R_{det}$ . (6) Detection radius. (7) Global spectroscopic XMM-Newton temperature, non core excised. (8) Detection of strong lensing in the CFHT data.

Cluster	RA (J2000)	Dec (J2000)	$z$	$L_X[0.1, 2.4]\text{keV}$ ( $h_{70}^{-2} 10^{44} \text{ erg s}^{-1}$ )	$R_{det}$ (arcmin)	$kT$ (keV)	strong lens (Y/N)
MS 0015.9+1609	00 <sup>h</sup> 18 <sup>m</sup> 33.26 <sup>s</sup>	+16°26′12.9″	0.541	16.3 ± 0.1	5.1	9.0 ± 0.2	N
MS 0451.6–0305	04 <sup>h</sup> 54 <sup>m</sup> 10.85 <sup>s</sup>	−03°00′57.0″	0.537	15.2 ± 0.1	3.7	8.8 ± 0.3	Y
RXC J0856.1+3756	08 <sup>h</sup> 56 <sup>m</sup> 12.69 <sup>s</sup>	+37°56′15.0″	0.411	4.25 ± 0.1	3.8	6.9 ± 0.4	N
RX J0943.0+4659	09 <sup>h</sup> 42 <sup>m</sup> 56.60 <sup>s</sup>	+46°59′22.0″	0.407	4.56 ± 0.1	4.1	5.4 ± 0.2	N
RXC J1003.0+3254	10 <sup>h</sup> 03 <sup>m</sup> 04.62 <sup>s</sup>	+32°53′40.6″	0.416	2.80 ± 0.2	3.5	3.6 ± 0.2	N
RX J1120.1+4318	11 <sup>h</sup> 20 <sup>m</sup> 07.47 <sup>s</sup>	+43°18′06.0″	0.612	5.82 ± 0.3	2.1	5.2 ± 0.3	N
RXC J1206.2–0848	12 <sup>h</sup> 06 <sup>m</sup> 12.13 <sup>s</sup>	−08°48′03.6″	0.441	20.7 ± 0.1	6.4	9.5 ± 0.2	Y
MS 1241.5+1710	12 <sup>h</sup> 44 <sup>m</sup> 01.46 <sup>s</sup>	+16°53′43.9″	0.549	6.86 ± 0.2	3.5	4.6 ± 0.1	N
RX J1347.5–1144	13 <sup>h</sup> 47 <sup>m</sup> 32.00 <sup>s</sup>	−11°45′42.0″	0.451	41.8 ± 0.1	4.9	11.4 ± 0.2	Y
MS 1621.5+2640	16 <sup>h</sup> 23 <sup>m</sup> 35.16 <sup>s</sup>	+26°34′28.2″	0.426	5.09 ± 0.9	4.2	5.8 ± 0.7	Y
RX J2228.5+2036	22 <sup>h</sup> 28 <sup>m</sup> 33.73 <sup>s</sup>	+20°37′15.9″	0.412	13.3 ± 0.1	8.8	7.8 ± 0.3	N

to realistic simulations of data. We describe below the details of how we implemented our weak lensing pipeline up to the measure of the total mass of the clusters.

### 3.1. Objects selection

The very first step of any weak lensing analysis consists in detecting and sorting galaxies and stars. This is explained in details in Paper 1, a methodology that is summarized as follows. Using SExtractor in dual mode, we detect the objects on the  $\chi_{gri}^2$  image while astrometric and photometric parameters are measured on each individual  $g'$ ,  $r'$ ,  $i'$  and  $z'$  images. Stars, galaxies and false detections are sorted according to several criteria: position in the magnitude/central flux diagram which displays the *star branch*, size with respect to the size of the PSF, and stellar index, according to the CLASS\_STAR parameter. Objects in masked area are also removed. After this selection step, galaxy densities are of the order of 30 arcmin<sup>-2</sup>, and the completeness magnitude ranges from 24.5 to 25 in the  $r'$  band, depending on the data quality in the different cluster fields.

In order to correct for the PSF smearing, we use the Im2SHAPE software (Bridle et al. 2002), which has already demonstrated its potential to recover the intrinsic shape of the galaxies (Cypriano et al. 2004; Bardeau et al. 2005, 2007; Limousin et al. 2007a,b). Starting with a given model for the shape of each object, the code convolves it with the local estimate of the PSF. For simplicity, both the PSF and the object are modeled with a single elliptical gaussian profile. Exploring the space parameters with a MCMC sampler, the most likely model is found by minimizing the residuals, the whole distribution being used to estimate robust statistical errors on each parameter.

We first determine the local PSF by looking at the shape of the stars. The resulting PSF field is cleaned and smoothed by looking at the 10 nearest stars at each point and removing those that differ by more than  $1.5\sigma$  from the local average shape. This ensures to avoid any jump in the PSF pattern, e.g. near masked area. We also exclude objects having an ellipticity larger than 0.2, thus reducing the contamination of the stars catalog by false detections and faint galaxies. The PSF map over the whole field of view is then obtained by averaging the ellipticities of the 5 nearest stars at each galaxy position. We checked that our Im2SHAPE implementation can recover point-like objects by applying this PSF correction to each star. Figure 2 shows the results of the shape parameters measurements for these stars: the

size distribution is dominated by point-sources and the orientation is more uniformly distributed after the PSF correction. It is also shown Figure ?? where the regular pattern of the stars ellipticities due to the PSF (top row) disappear after the deconvolution.

### 3.2. Validation of the shape measurements with simulated data

To check the performance of our Im2SHAPE implementation, we tested our pipeline on the simulated fields provided by the STEP collaboration (the Shear Testing Programme, Heymans et al. 2006). STEP1 simulations were built in order to compare the accuracy of different lensing pipelines for ground-based images. They provide a set of images reproducing CFHT-like observations with representative densities of stars and galaxies. These simulations combine several PSF models and shear intensities. We ran our lensing pipeline on each corresponding data set, compare our results to the input configurations and derive an average shear calibration bias and PSF residual.

Our implementation of Im2SHAPE differs slightly from the one proposed by S. Bridle in the STEP1 simulations: for simplicity and efficiency we fitted both the PSF and the galaxy shapes by a single elliptical gaussian instead of 2 concentric ones. This avoids to deal with 2 different values of the galaxies ellipticity when measuring the shear profiles. Despite this simplification, our method is very satisfactory as we obtain a calibration bias  $\langle m \rangle \simeq -0.1 \pm 0.02$  and a PSF residual  $\sigma_c \simeq 2.10^{-3}$ , a value consistent with shot noise (see eq. 11 of Heymans et al. 2006). These two values can be compared to the results from other weak lensing methods that are summarized on Figure 3 of Heymans et al. (2006). So in the present case we introduce an underestimation of the true shear around 10% but with no significant systematics. In the rest of the paper we will therefore increase all measures of the shear by a 10% factor before we use them to derive cluster masses.

### 3.3. Shear radial profiles

To quantify the shape of a galaxy, we use the complex ellipticity defined by Bonnet & Mellier (1995). It relates the tensor of the galaxy brightness second moments to its shape. Applying the lensing transformation between the source and image planes,

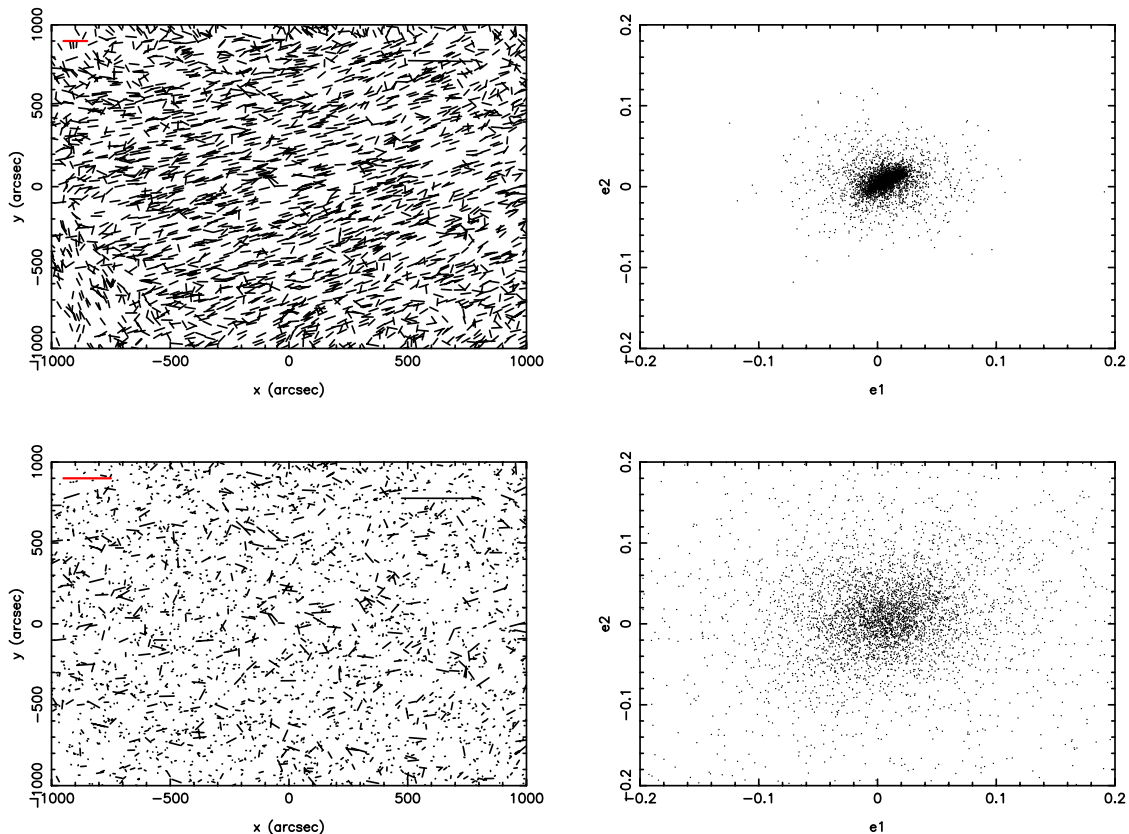


**Fig. 1.** PSF treatment applied to stars: on the top-left panel we show the stars ellipticity before the `Im2SHAPE` deconvolution. The corresponding distribution in terms of ellipticity components ( $e_1, e_2$ ) is shown in the top-right panel. Bottom-left panel shows the stars after the deconvolution by the PSF field (see text) and the bottom-right panel the corresponding distribution of ( $e_1, e_2$ ), which is more uniformly distributed than before the deconvolution. In both left panels is shown in red the scale corresponding to a semi-major axis of  $1''$ .

one find the simple relation (Seitz & Schneider 1997):

$$e^{(s)} = \begin{cases} \frac{e - g}{1 - g^* e} & \text{for } |g| \leq 1 \\ \frac{1 - g e^*}{e^* - g^*} & \text{for } |g| > 1 \end{cases} \quad (1)$$

where  $*$  denotes the complex conjugate,  $e^{(s)}$  being the complex ellipticity in the source plan and  $e$  in the image plan.  $g$  is the reduced shear

$$g = \frac{\gamma}{1 - \kappa} \quad (2)$$

which is a non-linear function of the two lensing functions: the (complex) shear  $\gamma$  and the convergence  $\kappa$  which is related to the projected mass density.

We assume spherical symmetry of the mass distribution and we consider that unlensed galaxies are randomly oriented on the sky plane. This is observationally confirmed since the distribution of the field galaxy ellipticities can be fitted by a gaussian  $\mathcal{N}(0, \sigma_e^2 \approx 0.25^2)$  (Tyson & Seitzer 1988; Brainerd et al. 1996). In the weak lensing approximation (i.e.  $\kappa \ll 1$ ) we get an unbiased estimator of the reduced shear by averaging the shape of background galaxies in concentric annuli around the cluster center. Spherical symmetry also implies that the averaged radial component of the shear vanishes, i.e.  $\langle e_{\perp} \rangle = 0$ , while the tangential component of the lensed galaxies traces the reduced shear  $\langle e_{\parallel} \rangle = g$ . We also assume that  $\langle e^{(s)} \rangle = 0$  with an intrinsic

dispersion  $\sigma_e \approx 0.25$ . The measure of this averaged tangential component ( $e_{\parallel}$ ) at different distances provides a reduced shear profile  $g(r)$  which is used to recover the total mass of the deflector.

We fix the center of the lens at the position of the brightest galaxy (BCG). The non-parametric mass reconstructions of the cluster sample that will be presented in Paper 2, show separations between the cluster mass center and the location of the BCG smaller than  $30''$  for all clusters except the most disturbed ones or those with a low S/N mass reconstruction. Real shifts between the BCG and the mass center are expected, especially in the most massive dark matter haloes or in non-relaxed clusters (see e.g. Skibba et al. 2011 for a discussion of the central galaxy paradigm). However, Dietrich et al. (2011) also showed with simulated data that for mass reconstructions done with ground-based data, shifts are observed with a median value of  $1'$  between the true and the reconstructed mass center. So here we can not reliably disentangle artefacts in the 2D mass reconstructions from real shifts between the BCG and the mass center. Moreover, given the redshifts and mass of the clusters, small miss-centerings disturb only the central data points in the shear profile. As discussed in Mandelbaum et al. (2010), excluding the central parts of the profiles in the fitting procedure reduces the underestimation of the mass because of miss-centering. Basic simulations (lensing a typical catalog of sources by a cluster representative of the sample in terms of mass and redshift) show that our fitting methodology gives consistent masses within their error bars up to top miss-centering of  $1'$ . Therefore we consider that

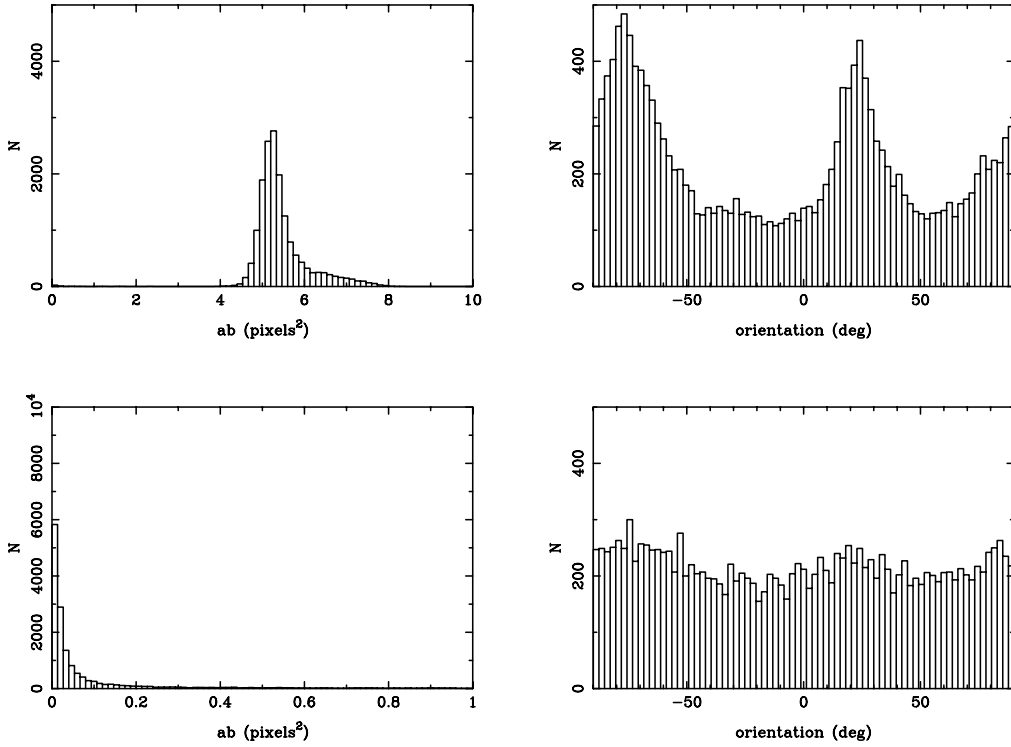


**Fig. 2.** Distribution of the area (left) and orientation (right) of the stars selected in the field of RX J2228.5+2036. The top panels represent the stars before the PSF deconvolution by IM2SHAPE while the bottom panels show the distribution after deconvolution, with an average size close to point-like objects and a uniform orientation of the stars.

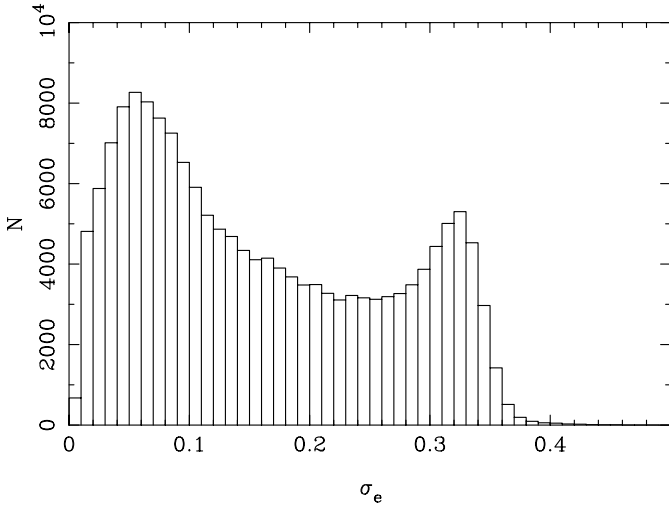


**Fig. 3.** Distribution of the errors on the galaxies ellipticity estimator given by IM2SHAPE (here for RX J2228.5+2036). The minimum of the histogram is reached for an uncertainty  $\sigma_e \sim 0.25$ . This value gives a natural cut to clean up the catalogs of galaxies used to measure the shear profiles.

in our case the BCG is a good estimator of the actual mass center and that this assumption does not have any consequence on the total mass determination.

Shear profiles are built in non-overlapping logarithmic annuli with  $r_{out} = 1.2r_{in}$ , in order to have similar S/N ratios in each bin. Thanks to the wide field images taken with Megacam, we are able to measure shear profiles up to 600 to 800'' from the BCG. We limit the fit of the shear profile in the central region to an inner radius set at 25'' (which roughly corresponds to the Einstein radius of the clusters) except for 4 clusters presenting a shear signal that is too disturbed in the central part. In these cases, the limit is fixed to the radius where the signal becomes significantly positive. This inner limit reduces the impact of miss-centering and avoids complications due to the non-linearity of the reduced shear with mass density. It also avoids the noise induced by galaxies which shape is badly estimated because they are too close to bright cluster galaxies (e.g. Cypriano et al. 2004).

Within these limits, 10 to 15 data points are available in the shear profile. In order to improve the statistical weight of the results, we have chosen to construct 25 *shifted* profiles by moving the position of the lower bound of the first bin by 1/25 of its width. This allows to reduce sampling effects in the first points of the profile where the averaged tangential ellipticity can significantly change according to the way the galaxies are binned. Each of these 25 profiles are fitted using a standard  $\chi^2$  minimization (**the distribution of field galaxies ellipticity being gaussian, e.g. Brainerd et al. (1996), the likelihood follows gaussian statistics**). Doing so, we limit the correlation that would arise with overlapping bins.

To improve the shear estimator, we weighted the average value of the tangential component of the galaxies ellipticity with the inverse of the ellipticities distribution variance  $\omega_j = 1/\sigma_{\parallel,j}^2$ :

$$g_i = \frac{\sum_{j=0}^{N_i} \omega_j e_{\parallel}^j}{\sum_{j=0}^{N_i} \omega_j}. \quad (3)$$

$\sigma_{\parallel}$  is the quadratic sum of the errors ( $\sigma_{e1}, \sigma_{e2}$ ) given by IM2SHAPE for each object and the intrinsic dispersion of the galaxies ellipticities  $\sigma_{int} = 0.25$ . Note that we also cut our catalogs of galaxies by limiting the uncertainties returned by IM2SHAPE to  $(\sigma_{e1}, \sigma_{e2}) < 0.25$ . This value corresponds to the average minimum in the uncertainties distributions (Figure 3), the objects above this threshold being most likely false detections or very faint/small galaxies. Note also that thanks to our weighting scheme their removal does not have any consequences on the final mass estimates (see Cypriano et al. 2004 for details).

To assess the uncertainties on the best fit parameters, we proceed as follow. Assuming that the measures  $g_i$  have a gaussian uncertainty  $\sigma_i$  (although the distribution of the errors appears to be highly non-gaussian on Figure 3, ellipticities for each galaxy generated by IM2SHAPE have a gaussian distribution), we generated 1000 Monte Carlo draws of each of the 25 shifted shear profiles, and applied the  $\chi^2$  procedure. We then obtain 25000 values of the best fit parameters. The mode of the resulting distribution gives the most likely solution along with the 1, 2 and 3  $\sigma$  asymmetric errors.

### 3.4. Normalization of the shear profiles

To limit the contamination of the sources catalogs we introduce several magnitude and color cuts which are discussed in details in Paper 2. In summary, we limit the magnitude range to  $21 - m_{\text{comp}} + 0.5$  in  $r'$  and remove all objects located within a color-band defined by the bright ellipticals red sequence up to  $m_r = 23$ . This reduces the galaxy density by about 1/3 even if some contamination by bluer galaxies remains. To overcome this problem, we followed the method proposed by Hoekstra (2007) which assumes that the number density of cluster members simply decreases with radius as  $1/r$ . We adjust the normalization by fitting the profile of galaxies excess relative to the background level and we correct the measured shear according to the distance to the cluster center (Figure 4). As the richness of a cluster scales with its mass, this contamination is higher for more massive objects. So we apply the renormalization procedure for each cluster instead of using an average correction as done in Hoekstra (2007).

Photometric redshift information is also necessary to correct for two effects which change the normalization of the shear profiles. The first one is an assessment of the fraction of foreground galaxies in the catalogs and the second one is the determination of the average redshift distribution of the background sources. To get a reliable faint galaxies redshift distribution, we used the photometric redshifts of galaxies in reference fields, neglecting the cosmic variance between different fields (Cypriano et al. 2004; Hoekstra 2007; Limousin et al. 2009; Oguri et al. 2009). Observations in the CFHTLS Deep fields obtained with the same instrument form the ideal data set for our study (Gavazzi & Soucail 2007). They are much deeper than the present observations so we can consider that their catalogs are complete up to our magnitude limit. We used the photometric redshifts determined with the HYPERZ software (Bolzonella et al. 2000). They were calibrated and validated by comparison with spectroscopic redshifts obtained in the VVDS D1 field (Le Fèvre et al. 2005)

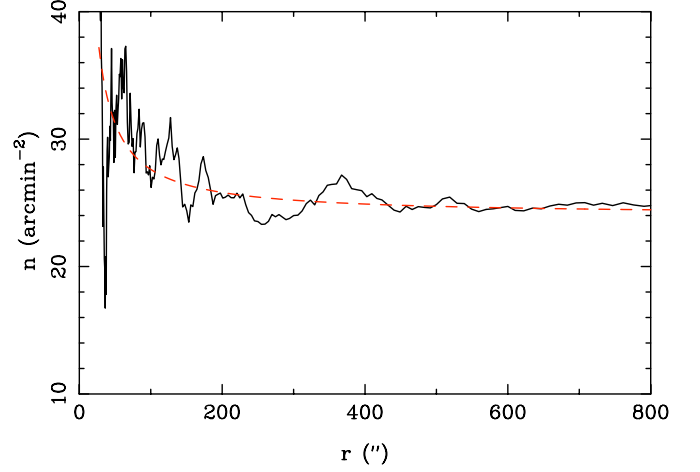


**Fig. 4.** Density profile of the background galaxies used for the fit of the shear profile in the field of MS 1621.5+2640. Despite the removal of the galaxies within the red sequence, a substantial fraction of cluster members remains. The density profile is fit (dashed red line) to give the boosting factor applied to the shear profile.

and in the Growth Deep survey (Weiner et al. 2005). Once our photometric selection criteria were applied on the CFHTLS catalogs, we obtained a redshift distribution that is supposed to be representative of the catalogs we use for the weak lensing analysis.

We use this distribution of photometric redshifts to determine the strength of the shear signal via the geometrical factor  $\beta(z_L, z_S) = D_{LS}/D_{OS}$  ( $D_{LS}$  is the angular-diameter distance between the lens and the source and  $D_{OS}$  the distance to the source). Both the convergence  $\kappa$  and the shear  $\gamma$  can be re-written as (Hoekstra et al. 2000):

$$g = \frac{\gamma}{1 - \kappa} = \frac{\beta_s \gamma^\infty}{1 - \beta_s \kappa^\infty} \quad (4)$$

with  $\beta_s = \beta/\beta^\infty$  and  $\beta^\infty, \gamma^\infty, \kappa^\infty$  are the corresponding functions for a source at infinity. In the weak lensing approximation,  $g \approx \gamma$ , the redshift dependence of the signal is easy to take into account as the average reduced shear simply equals its value taken with the average geometrical factor.

For galaxy clusters at low redshift, it is straightforward to replace  $\langle \beta \rangle$  by the  $\beta$  value of an average redshift  $z_s$ , usually set to 1 (Okabe & Umetsu 2008; Radovich et al. 2008). In the present case, the geometrical factor varies significantly with the sources redshifts so we computed the factor  $\langle \beta(z) \rangle$  for the whole distribution of field galaxies. We account for the contamination by foreground galaxies given our selection criteria by setting  $\beta(z_{\text{phot}} < z_{\text{cluster}}) = 0$  (values in a range of 20% to 30% depending on the cluster). Note that such an approach is only valid in the weak lensing regime because of the non-linearity of the reduced shear with  $\beta$  (see e.g. Seitz & Schneider 1997; Hoekstra et al. 2000). However, as with remove the central parts from the fits, we expect these  $\langle \beta(z) \rangle$  to be a good approximation. The averaged geometrical factors are given in Table 2 along with the effective redshift defined as  $\beta(z_{eff}) = \langle \beta(z) \rangle$ .

**Table 2.** Summary of the weak lensing analysis. Columns are (1) cluster name; (2-3) NFW masses; (4) SIS velocity dispersion; (5) Einstein radius for a source at  $z_s = 2$ ; (6-7) radius corresponding to the NFW masses; (8) average geometrical factor corrected from dilution (see text); (9) effective redshift derived from the average geometrical factor.

Cluster	$M_{200}$ ( $10^{15} h_{70}^{-1} M_{\odot}$ )	$M_{500}$ ( $10^{15} h_{70}^{-1} M_{\odot}$ )	$\sigma_v$ (km.sec $^{-1}$ )	$\theta_E$ ( $''$ )	$R_{200}$ ( $h_{70}^{-1}$ kpc)	$R_{500}$ ( $h_{70}^{-1}$ kpc)	$\langle \beta \rangle$	$z_{eff}$
MS 0015.9+1609	$2.56^{+0.49}_{-0.41}$	$1.77^{+0.34}_{-0.29}$	$1490^{+90}_{-90}$	$39^{+5}_{-5}$	$2330^{+130}_{-130}$	$1520^{+90}_{-90}$	0.26	0.78
MS 0451.6–0305	$1.44^{+0.30}_{-0.26}$	$1.00^{+0.21}_{-0.18}$	$1280^{+70}_{-90}$	$29^{+3}_{-4}$	$1920^{+120}_{-120}$	$1250^{+80}_{-80}$	0.27	0.79
RXC J0856.1+3756	$0.78^{+0.12}_{-0.15}$	$0.54^{+0.09}_{-0.11}$	$1000^{+50}_{-70}$	$20^{+2}_{-3}$	$1650^{+80}_{-120}$	$1070^{+50}_{-70}$	0.39	0.73
RX J0943.0+4659	$0.93^{+0.18}_{-0.21}$	$0.64^{+0.12}_{-0.15}$	$1090^{+60}_{-100}$	$24^{+3}_{-4}$	$1770^{+90}_{-160}$	$1150^{+60}_{-100}$	0.38	0.72
RXC J1003.0+3254	$0.74^{+0.18}_{-0.13}$	$0.51^{+0.13}_{-0.09}$	$990^{+70}_{-70}$	$19^{+3}_{-3}$	$1690^{+90}_{-140}$	$1100^{+60}_{-90}$	0.37	0.72
RX J1120.1+4318	$0.59^{+0.26}_{-0.15}$	$0.41^{+0.18}_{-0.10}$	$1020^{+90}_{-110}$	$17^{+3}_{-4}$	$1460^{+130}_{-150}$	$950^{+100}_{-100}$	0.23	0.85
RXC J1206.2–0848	$1.51^{+0.28}_{-0.18}$	$1.05^{+0.19}_{-0.12}$	$1290^{+50}_{-60}$	$32^{+3}_{-3}$	$2030^{+110}_{-90}$	$1320^{+70}_{-60}$	0.36	0.75
MS 1241.5+1710	$1.39^{+0.30}_{-0.30}$	$0.96^{+0.20}_{-0.21}$	$1230^{+100}_{-90}$	$26^{+4}_{-4}$	$1880^{+130}_{-140}$	$1230^{+80}_{-90}$	0.27	0.81
RX J1347.5–1144	$2.56^{+0.32}_{-0.31}$	$1.77^{+0.22}_{-0.21}$	$1500^{+60}_{-60}$	$43^{+3}_{-3}$	$2400^{+100}_{-100}$	$1560^{+60}_{-60}$	0.35	0.76
MS 1621.5+2640	$1.23^{+0.20}_{-0.22}$	$0.85^{+0.14}_{-0.15}$	$1200^{+60}_{-80}$	$28^{+3}_{-4}$	$1900^{+100}_{-120}$	$1240^{+60}_{-80}$	0.38	0.75
RX J2228.5+2036	$0.85^{+0.21}_{-0.18}$	$0.59^{+0.14}_{-0.12}$	$1050^{+80}_{-80}$	$22^{+3}_{-3}$	$1680^{+130}_{-120}$	$1100^{+80}_{-80}$	0.39	0.75

## 4. Weak lensing masses

### 4.1. Mass models

We restrict our analysis to the two mostly used parametric mass models: the singular isothermal sphere (SIS hereafter) and the NFW model (Navarro et al. 1995). The SIS mass model is the most simple one to describe a relaxed massive sphere with a constant and isotropic velocity dispersion  $\sigma_v$ . The mass density profile writes as

$$\rho(r) = \frac{\sigma_v^2}{2\pi G r^2}$$

and simple expressions are derived for the lensing functions  $\gamma(r) = \kappa(r) = R_E/2r$  where the Einstein radius scales as  $R_E \propto \beta\sigma_v^2$ . This mass model is a poor description of the actual mass distribution of clusters. So the fitting results of this mass model will not be used to derive the total clusters mass in the rest of this work. However it allows easy comparisons with other mass estimators such the dynamical analysis of the galaxies members that are also characterized by a velocity dispersion  $\sigma_v$ . It also provide an estimate of the Einstein radius  $R_E$  which can be compared to results from strong lensing analysis. This latter quantity requires an estimate of the geometrical factor to be converted from  $\sigma_v$ . Values given in Table 2 are derived using a source redshift  $z_s = 2$  which leads to radii in the range  $20'' - 40''$  (note that these values are not directly estimated from the signal in the central part as done in strong lensing analysis but derived from the fit of the weak lensing shear profile).

The NFW mass profile (Navarro et al. 1997, 2004) was introduced to model the mass distribution of a cold dark matter halo formed in a gravitational scenario of structures formation. It involves a shape parameter, the concentration  $c$ , and a normalization parameter often expressed as the scale radius  $r_s$ :

$$\rho(r) = \frac{\rho_c \delta_c}{(r/r_s)(1 + r/r_s)^2}$$

$\rho_c$  is the critical mass density of the Universe at the redshift of the cluster and  $\delta_c$  is a dimensionless factor which is related to the contrast density of a virialized dark matter halo  $\Delta = \bar{\rho}/\rho_c = 200$  by

$$\delta_c = \frac{200}{3} \frac{c^3}{\ln(1+c) - \frac{c}{1+c}}$$

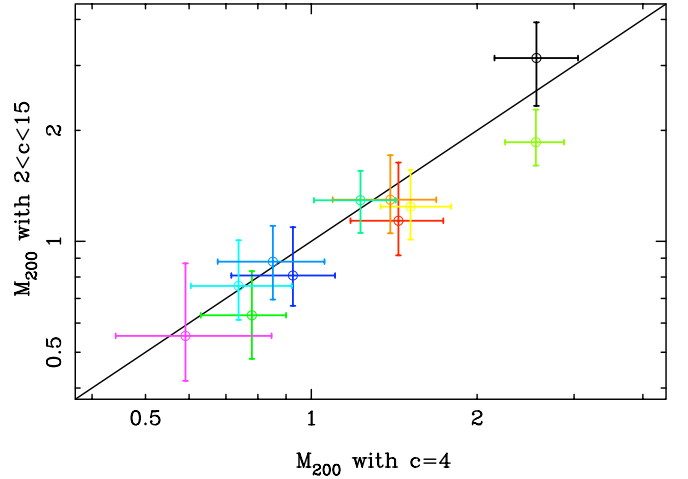


**Fig. 5.** Comparison between the total mass  $M_{200}$  (expressed in units of  $10^{15} h_{70}^{-1} M_{\odot}$ ) obtained by fitting the shear profile with a NFW model. In the first case the concentration parameter is fixed to  $c = 4$  while in the second case it is left as a free parameter varying over the range  $2 < c < 15$ , increasing the mass uncertainties by 25% typically.

We also define  $R_{200} = c r_s$ , often called the virial radius, and the mass enclosed within this radius

$$M_{200} = \frac{800 \pi}{3} \rho_c R_{200}^3$$

$\Delta = 200$  roughly corresponds to the virialized part of clusters. X-ray studies more often make use of  $\Delta = 500$ , a density contrast more easily reached by the X-ray detection. Given the above relations, it is straightforward to analytically switch masses and radii from one  $\Delta$  value to another.

With two free parameters, the NFW model provides more freedom to adjust the mass profile of galaxy clusters. However, there is a well-known degeneracy between the total mass  $M_{200}$  and the concentration parameter  $c$  when fitting the shear profile in the weak lensing regime. This comes from a lack of information on the mass distribution near the cluster center. The observed  $c - M$  degeneracy shows a much steeper slope than

the theoretical one (Okabe et al. 2010a) and only a combination of strong and weak lensing can raise it and provide useful constraints on the concentration parameter. In the present case, with no strong lensing modeling of all the clusters in the sample, we decided to fix the concentration parameter and only fit the total mass  $M_{200}$ . Indeed for most of the clusters, the fit of both parameters leads to unrealistic values of  $c$ , either larger than 20 or, in most cases, stuck to the lower limit of the fit  $c = 2$ . Since a low concentration is associated to a lower mass when fitting a given shear profile, this leads to the apparent bias observed Figure 5, which is only an artefact due to poor constraints in the central parts of the shear profiles. For a more secure mass estimator we therefore fixed the concentration parameter  $c$  to a canonical value for massive clusters,  $c_{200} = 4$ , and fit the mass profile with only one free parameter.

It is interesting to note that the ratio between the NFW mass  $M_{200}$  and the SIS mass integrated within  $R_{200}$  is close to one for the whole sample:  $\langle M_{200}^{NFW}/M_{200}^{SIS}(R_{200}) \rangle = 0.98 \pm 0.06$ . This reflects the fact that in this study of high redshifts clusters of galaxies, weak lensing data only provide constraints on the total mass at large scales. It cannot efficiently constrain the radial mass profile contrary to clusters at lower redshifts where some disagreements are found between the 2 mass models (Okabe et al. 2010a).

In summary, we have in hands for each cluster the results of the fit by a SIS profile ( $\sigma_v$  and  $R_E$ ) as well as those by a NFW profile ( $M_{200}$  and  $R_{200}$ ). The mass and the radius taken at  $\Delta = 500$  are also computed for comparison with the results of the X-ray analysis. All these values are given in Table 2. Note that because we are interested here in the calibration of scalings relation and the scatter of individual clusters around the best fits, we do not have included the systematic uncertainty due to projection effects of the large scale structures. This effect should be less than 10% for rich clusters at intermediate redshifts (Hoekstra 2001). We also did not include the error on the geometrical factor  $\langle \beta \rangle$ . Its value varies in a range 3%–6% depending on the cluster when the different CFHTLS Deep fields are used to estimate it. Moreover, in the present case, these 2 quantities are second order effects and the main source of uncertainties remains the intrinsic ellipticity of the lensed galaxies (e.g. Hoekstra 2007).

#### 4.2. Comparison of the X-ray and weak lensing masses

Raw XMM-Newton data were processed as described in Pointecouteau et al. (2005) and Pratt et al. (2007). As for the REXCESS sample (Croston et al. 2008), surface brightness profiles were PSF-corrected, deprojected and converted to 3D density profiles using the non parametric method described in Croston et al. (2006). 2D temperature profiles were extracted from XMM-Newton spectroscopy as described in Pratt et al. (2010). The 3D profiles were recovered assuming analytical functions taking into account the PSF mixing effects and weighting the contribution of temperatures in various rings. A Monte Carlo procedure was used to compute the errors (Arnaud et al. 2010). The hydrostatic mass equation was then applied to the density and temperature profiles and to their logarithmic gradients to derive the observed mass profile for each cluster. Again a Monte Carlo method was applied to determine the errors on each point, taking into account over-constraints on the 3D profile imposed by the use of a parametric model. Observed mass profiles were finally fitted with a NFW profile, constraining the shape and the normalization parameters, i.e.  $c_{500}$  and  $M_{500}$ .

Figure 6 shows the comparison between the weak lensing and the hydrostatic equilibrium masses derived from the X-ray

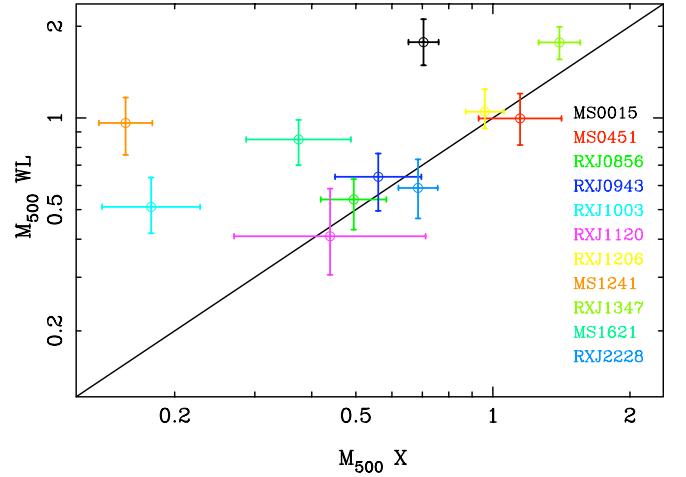


**Fig. 6.** Masses obtained with the weak lensing analysis (y-axis) versus the hydrostatic equilibrium masses obtained with the X-ray analysis (x-axis). All masses are given in units of  $10^{15} h_{70}^{-1} M_{\odot}$  and are computed at the density contrast  $\Delta = 500$ .

data for the 11 clusters. The comparison is made at a density contrast  $\Delta = 500$  to avoid any extrapolation of the X-ray data. The weak lensing masses  $M_{200}$  are simply converted into  $M_{500}$  assuming a concentration parameter  $c_{200} = 4$ . This means that we are not comparing weak lensing and hydrostatic masses evaluated in the same physical radius. We are instead focusing here on a raw comparison between fitting results.

Over the whole sample, we almost reach a  $1\sigma$  agreement between the 2 mass estimators since 7 clusters (i.e.  $\sim 64\%$ ) have compatible masses within their  $1\sigma$  interval of individual uncertainties, with a small scatter and no strong systematics, Fig. 7. With the 11 clusters, we obtain an average mass ratio  $\langle M_{WL}^{500}/M_X^{500} \rangle = 1.92 \pm 1.58$ . Removing MS 1241.5+1710 that is almost  $3\sigma$  away from this average ratio, we find  $\langle M_{WL}/M_X \rangle = 1.49 \pm 0.75$ , a value much less scattered. We recover here the 'classical' result that is a moderate excess for the weak lensing masses.

Similar studies were previously done on clusters at lower redshifts (Zhang et al. 2008; Mahdavi et al. 2008; Zhang et al. 2010), but it is the first time we show this kind of comparison at such a high redshift range. Unfortunately, the weak lensing mass profiles are not sufficiently constrained to allow a more detailed study of the variation with radius of the mass ratio  $M_{WL}/M_X$ . A combination with strong lensing information would be needed to overcome this difficulty. It will be explored in a forthcoming paper for the EXCPRES clusters for which strong lensing features are detected (4 out of the 11 clusters).

For the 4 outliers identified in Figure 6, their individual properties will be presented in Paper 2. However it remains difficult to fully understand on a case by case why these clusters show such discrepancies. It certainly results from the mixed effect of intrinsic physical departures from hydrostatic equilibrium and the limited quality of the lensing data. Some differences are also statistically expected in unbiased samples of clusters and can be characterized with numerical simulations (Meneghetti et al. 2010). However, because of the limited size of the sample, we did not separate dynamically perturbed clusters from the relaxed one and try to highlight variations in the normalization and scatter of the  $M_{WL} - M_X$  relation.



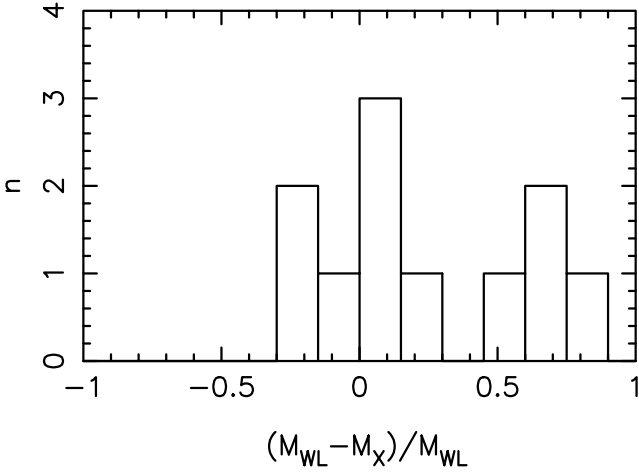


**Fig. 7.** Relative difference distribution between the weak lensing masses and the X-ray masses for the 11 clusters of our sample. Masses are given at the density contrast  $\Delta = 500$ .

## 5. Mass-observable correlations

### 5.1. Methodology

Because both masses and observables have uncertainties with possible correlations (e.g. the richness depends on  $R_{200}$  and thus on the total mass), a simple  $\chi^2$  minimization cannot be used to calibrate scaling relations. Moreover, we expect to have an intrinsic dispersion around the main scaling relation which needs to be included and evaluated. So we preferred to perform a linear regression using the orthogonal BCES estimators (*Bivariate Correlated Errors and intrinsic Scatter*, Akritas & Bershady 1996). This approach has already been used by several groups for the calibration of mass-observable scaling relations (Morandi et al. 2007; Pratt et al. 2009), expected to be characterized by power laws and so fitted by linear relations  $y = ax + b$  in the log-log plan. For each relation, both variables are normalized by a pivot close to their mean. This insures that the logarithmic slope and normalization of the relation are nearly independent parameters.

Once the best fit of the correlation is obtained, the total dispersion over the  $N$  points

$$\sigma_{tot}^2 = \frac{1}{N-2} \sum_{i=1}^N (y_i - \alpha x_i - B)^2 \quad (5)$$

equals the quadratic sum of the statistical dispersion  $\sigma_{stat}$  and the intrinsic one  $\sigma_{int}$ , which thus can be expressed as:

$$\sigma_{int}^2 = \frac{1}{N-2} \sum_{i=1}^N \left[ (y_i - \alpha x_i - B)^2 - \frac{N-2}{N} (\sigma_{y_i}^2 + \alpha^2 \sigma_{x_i}^2) \right] \quad (6)$$

For each relation, we also estimated the Spearman correlation coefficient  $\rho$ :

$$\rho = 1 - \frac{6 \sum d_i^2}{n(n^2 - 1)} \quad (7)$$

where  $d_i$  is the ranking difference of the  $i$ -th sorted mass and observable vector.  $\rho$  is a ranking correlation that shows the monotonic degree of the relation between the two variables ( $\rho = -1$  for a strictly decreasing relation,  $\rho = +1$  in the opposite case). Compared to the classical Pearson coefficient, the Spearman coefficient does not depend on the slope of the correlation. Such

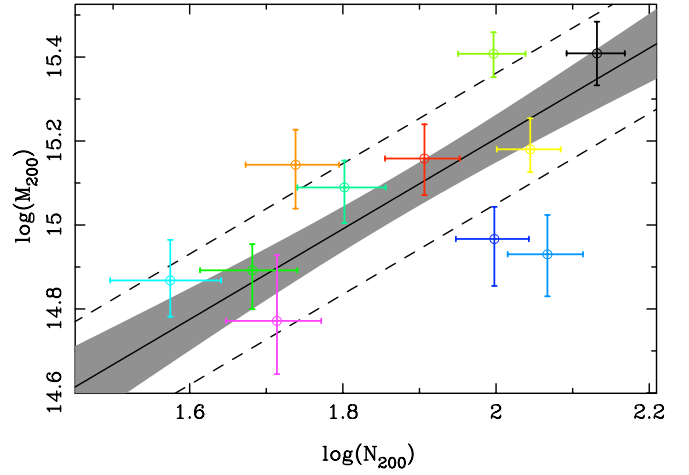


**Fig. 8.** Mass-richness scaling relation calibrated with the NFW lensing masses  $M_{200}$ . The black line shows the best BCES orthogonal fit. The region delimited by the two dashed lines corresponds to the intrinsic dispersion of the galaxy clusters around the best fit. The shaded area gives the statistical  $1\sigma$  uncertainty given by the best fit parameters.

a coefficient has been used in similar studies to quantify the strength of a correlation, e.g. Lin et al. (2004).

### 5.2. Optical scaling laws

First, we compared the weak lensing mass  $M_{200}$  to the optical richness  $N_{200}$ . We define  $N_{200}$  as number of galaxies within  $R_{200}$  that belong to the cluster red sequence (the precise definition will be presented in Paper 2). We keep only the brightest members with  $L < 0.4L^*$ .  $L^*$  is derived from the values of Ilbert et al. (2005) and according to the cluster redshifts. Richnesses are corrected from the background contamination but are not corrected from any luminosity cut nor any color selection. The aim is to remain consistent with previous studies that focus on the bright elliptical cluster galaxies.

The BCES calibration of this  $M_{200} - N_{200}$  relation, given in Table 3, presents a correlation with a logarithmic slope  $\alpha = 1.04 \pm 0.38$  (Fig. 8). Despite a rather large uncertainty, the slope is very close to 1, in agreement with the simplest model of structures formation (Kravtsov et al. 2004). The uncertainties of the BCES fit are dominated by the intrinsic dispersion (dashed lines) due to the limited size of the cluster sample and increased by one outlier, RX J2228.5+2036. These results are coherent with previous studies conducted at lower redshifts (Becker et al. 2007; Johnston et al. 2007; Reyes et al. 2008; Rykoff et al. 2008; Mandelbaum et al. 2008; Rozo et al. 2009). We also compared the X-ray masses with the cluster richnesses. This leads to a correlation with a slope  $\alpha = 1.14 \pm 0.18$ . In addition, we also looked at a possible correlation between the mass and the richness evaluated in a given physical radius. In practice, we used the richness determined within 1 Mpc (roughly equal to  $0.5R_{200}$ ). The BCES estimator gives a slope  $\alpha = 1.60 \pm 0.92$ , a result with a very large uncertainty that is useless with the present data.

To compare these different approaches, we computed the relative error  $R = |(M_{WL} - M_{pro.xy})/M_{WL}|$  averaged over the sample of clusters after removing the main outlier RX J2228.5+2036. The  $M - N_{200}$  relation leads to  $R = 0.27$  while with the  $M - N_{1 \text{ Mpc}}$  relation we find  $R = 0.41$ . Even if the conversion between richness and mass within a fixed aperture is less physical than the

use of the virial radius  $R_{200}$ , we show here that it is still acceptable. Clearly the uncertainties in the scaling relations are dominated by the intrinsic dispersion more than by the choice of the working radius (see also Andreon & Hurn 2010). The accurate determination of  $R_{200}$  is a second order effect and the use of a simple fixed aperture for the measure of the cluster richness can already lead to a correct mass proxy. This is particularly true as our sample covers a restricted interval in both mass and redshift, so the fixed aperture is not far from a fixed density contrast.

Second, we tested the relationship between mass and optical luminosity. The  $M - L$  correlation gives a roughly constant mass-to-light ratio as the BCES estimator returns a slope  $\alpha = 0.95 \pm 0.37$ . Note that to be consistent with other similar works, we do not correct the total luminosities from incompleteness. Our catalogs are limited to  $0.4L^*$  and a correcting factor of  $\sim 1.6$  should be included to get the total luminosity, assuming a standard Schechter luminosity function. This is done in Paper 2 which discusses in details the M/L ratio of the clusters.

The correlation between X-ray masses and optical luminosities gives  $\alpha = 1.20 \pm 0.20$ , a value also compatible with a constant mass-to-light ratio. Note that, as for the  $M - N$  relation, the calibration with the X-ray masses gives a smaller intrinsic dispersion.

Previous studies tend to find a slope in the  $M - L$  relation slightly larger than 1 (Lin et al. 2004; Popesso et al. 2005; Bardeau et al. 2007; Reyes et al. 2008). This tendency is predicted by some of the semi-analytical models of galaxy formation, at least for massive clusters (Marinoni & Hudson 2002) in which the star formation efficiency can be inhibited by the long cooling times of hot gas on large-mass scales. Merging processes and galaxies interactions can also affect the luminosity of galaxies and are more efficient in massive clusters. But because of the small mass range covered by our cluster sample, it is difficult to draw firm conclusions on any possible variation of the M/L ratio with mass. It would be necessary to add galaxy groups in the sample, although accurate mass determinations are quite difficult for low mass structures.

Moreover, the complex method to determine the value of  $R_{200}$  represents an issue to estimate  $L_{200}$ . So we repeated the same procedure as described above and compared the masses with luminosities integrated inside a 1 Mpc radius. We also calculated the average relative errors on the mass. We obtain  $R = 0.47$  for masses derived from the  $M - L_{1\text{Mpc}}$  relation while we get  $R = 0.33$  when we use the  $M - L_{200}$  relation. Again, the intrinsic dispersion is the main source of uncertainties, the precise determination of  $R_{200}$  being a second order effect.

### 5.3. X-ray scaling laws

We focus here only on scaling laws fitted with the weak lensing masses taken at  $\Delta = 200$ . The calibration of the  $L_X - M$  relation has been the subject of many studies, mainly at low redshifts. Mass estimators are usually derived from X-ray data (Markevitch 1998; Arnaud et al. 2002; Reiprich & Böhringer 2002; Popesso et al. 2005; Morandi et al. 2007; Pratt et al. 2009; Vikhlinin et al. 2009). Several attempts to use weak lensing masses were also proposed more recently (Hoekstra 2007; Bardeau et al. 2007; Rykoff et al. 2008; Leauthaud et al. 2010; Okabe et al. 2010b). Most these studies converge towards a power law that differs from the relation expected in the hierarchical scenario of structures formation where the X-ray luminosity scales with the mass as  $F_z^{-1} L_X \propto (F_z M_{tot})^{4/3}$ . The  $F_z$  factor stands for the evolution of the scaling relation and reduces to  $h(z)$ , the reduced Hubble constant, for models of structures for-

mation based only on gravitation and assuming a fixed density contrast to derive masses (Voit 2005).

Several processes can affect the properties of a cluster, both generating an intrinsic dispersion around the expected  $L_X - M$  relation and a breaking of self-similarity. Most of previous studies point towards a slope that is slightly larger than the expected one, i.e.  $\alpha = 1.6 - 1.8$  instead of  $4/3$ . The intrinsic dispersion is found to be quite large, up to almost 50% (Reiprich & Böhringer 2002). However, it appears that when cool cores are removed, this intrinsic dispersion is smaller (Allen 1998; Markevitch 1998; Voit et al. 2002; Maughan 2007; Pratt et al. 2009). Indeed, the X-ray luminosity is strongly affected by the physical mechanisms ruling the baryonic content of clusters (pre-heating, radiative cooling, feedback of supernovae and active galactic nuclei ...), and so is the  $L_X - M$  with respect to the simplest gravitational model. These processes are modeled in up-to-date numerical simulations that combine the gravitational evolution of dark matter structures with the hydrodynamical behavior of the intra-cluster gas (Borgani et al. 2004; Kay 2004; Borgani 2008). These simulations also seem to favor a slope of the  $L_X - M$  relation larger than the canonical one.

The results of the BCES estimator for the  $L_X - M_{200}^{WL}$  relation are presented in Table 3. Although our  $L_X$  measurements do not purely equate  $L_{X,200}$  (see Table 1), our best fit relation is in good agreement with previous works as we find a slope  $\alpha = 2.06 \pm 0.44$ . Despite a strong correlation, we also observe a large scatter around the best fit with  $\sigma_{int} = 0.19$ .

These encouraging results should nonetheless be taken with caution as our sub-sample of the EXCPRES clusters was designed to keep only the most luminous clusters in the sample. It therefore covers a limited range in X-ray luminosity. In order to explore a larger range, we combined this sample with clusters from two studies: the COSMOS galaxy groups analyzed in Leauthaud et al. (2010) and the maxBCG galaxy groups and clusters presented in Rykoff et al. (2008) (Fig. 9). Both are using stacks of objects with similar richness to improve the statistics of the shear profiles for low mass objects. Their X-ray luminosities are also stacked within  $R_{200}$  apertures, whereas our values of the luminosities are computed within the detection radius (see Table 1). However, we checked that the ratio between  $R_{det}$  and  $R_{200}$  for our sample is  $\sim 0.9$  on average. We therefore consider that the present values are close enough to the values within  $R_{200}$ , thus allowing us to compare and combine them with the aforementioned works. This combination of the three data sets allows to cover an extended range in mass and luminosity. We fit them simultaneously and the best fit relation gives a slope of  $\alpha = 1.57 \pm 0.07$ . This slope is lower than that from our data only but still in disagreement with the hierarchical prediction of  $4/3$ . The intrinsic dispersion stays roughly unchanged over the combined sample.

Although it is not nowadays much used as a mass proxy, we then checked the  $M_{WL} - T$  relation. We derived a slope of  $\alpha = 1.33 \pm 0.42$ , a value compatible with the self-similar prediction of 1.5 within the  $1\sigma$  limit. This weak lensing calibration is compatible with those by Hoekstra (2007) and Okabe et al. (2010b), who respectively derive a slope of  $\alpha = 1.34 \pm 0.29$  and  $\alpha = 1.49 \pm 0.58$ .

We also computed the average relative error  $R$  between the weak lensing masses and the mass proxies determined with X-ray data. The  $L_X - M$  relation gives  $R = 0.28$  and the  $M - T$  lead to  $R = 0.31$ . These two values are of the same order of those previously obtained for the  $M - N$  and  $M - L$  correlations with optical data.

**Table 3.** Summary of the fitting results for the mass-observable scaling relations. Columns are (1) scaling relation; (2) best fit logarithmic slope; (3) best fit normalization; (4-5-6) total-statistic-intrinsic logarithmic dispersions; (7) Spearman coefficient. Masses are expressed in units of  $10^{15} h_{70}^{-1} M_{\odot}$  (except for the  $L_X - M$  relation with masses in units of  $5 \times 10^{14} h_{70}^{-1} M_{\odot}$ ). The optical luminosities are given in units of  $7 \times 10^{12} h_{70}^{-2} L_{\odot}$ , the richness is normalized to 80 and the temperature to 5 keV. X-ray luminosities are given in units of  $10^{45} h_{70}^{-2} \text{erg s}^{-1}$ .

scaling law	$\alpha$	$A$	$\sigma_{raw}$	$\sigma_{stat}$	$\sigma_{int}$	$\rho$
$M_{200}^{WL} - N_{200}$	$1.04 \pm 0.38$	$1.27 \pm 0.12$	$0.17 \pm 0.05$	$0.11 \pm 0.01$	$0.13 \pm 0.06$	0.66
$M_{200}^{WL} - L_{200}$	$0.95 \pm 0.37$	$1.28 \pm 0.20$	$0.18 \pm 0.04$	$0.10 \pm 0.01$	$0.14 \pm 0.05$	0.64
$h(z)^{-1} L_X - h(z) M_{200}^{WL}$	$2.06 \pm 0.44$	$0.29 \pm 0.07$	$0.27 \pm 0.06$	$0.16 \pm 0.03$	$0.19 \pm 0.08$	0.85
$h(z) M_{200}^{WL} - kT$	$1.33 \pm 0.42$	$1.03 \pm 0.20$	$0.15 \pm 0.04$	$0.09 \pm 0.01$	$0.12 \pm 0.05$	0.73

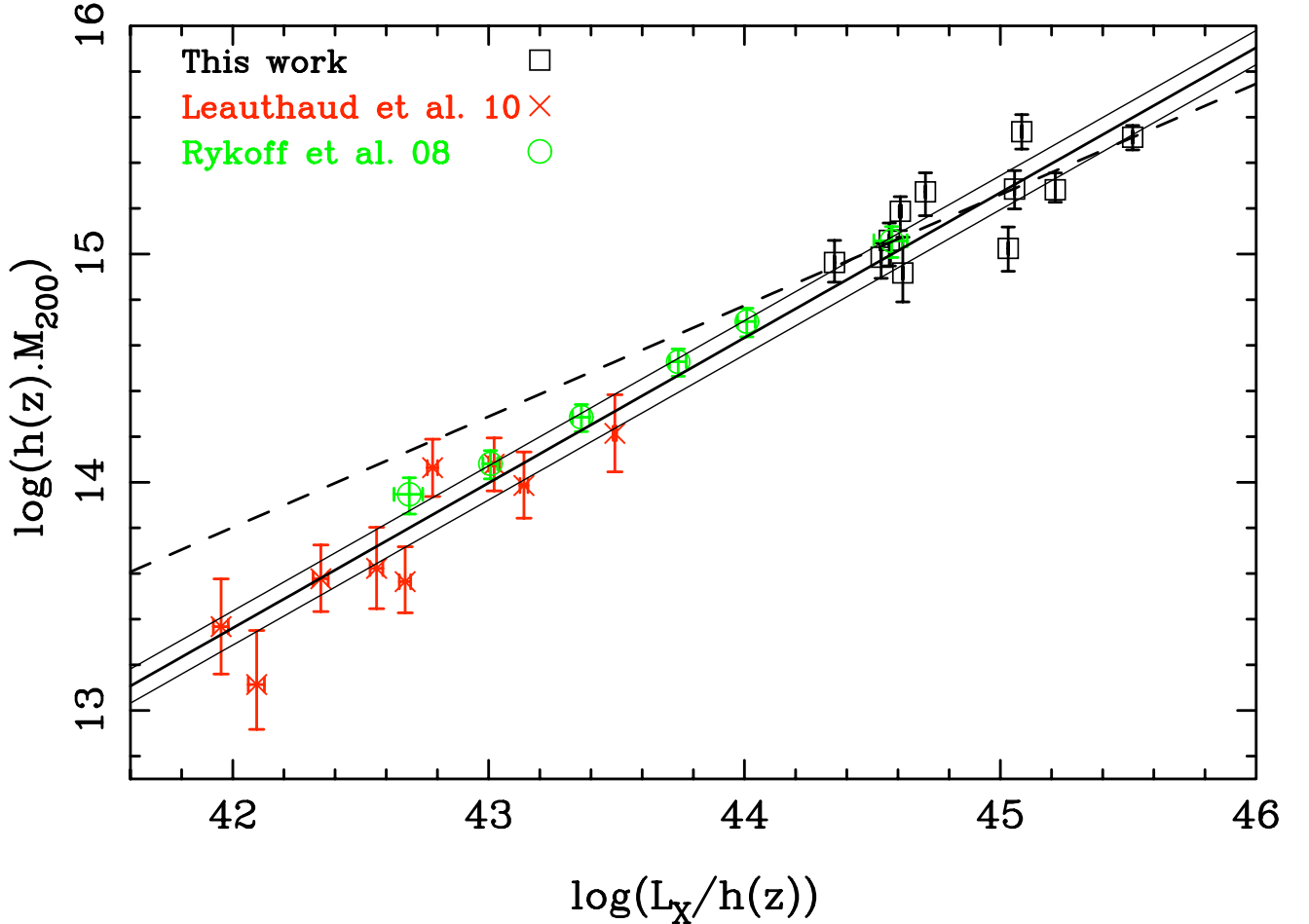


**Fig. 9.** Weak lensing masses versus X-ray luminosities using the EXCPRES clusters (black boxes) combined with the stacked clusters and groups of Rykoff et al. (2008) (green circles) and of Leauthaud et al. (2010) (red crosses). The solid lines show the best BCES fit and the corresponding intrinsic dispersion for the three data sets. For comparison the BCES best fit obtained with the EXCPRES weak lensing sub-sample only is plotted (dashed line).

## 6. Summary and conclusions

In this paper we provide for the first time a thorough weak lensing analysis of a sample of 11 galaxy clusters (a sub-sample of the EXCPRES sample – Arnaud et al. in preparation) in a relatively high redshift range,  $0.4 < z < 0.6$ . We have conducted a careful validation of our weak lensing pipeline, thanks in particular to the STEP simulations which allowed to re-calibrate our shear measurements. The shear profiles were fitted with a NFW profile with a fixed concentration parameter  $c_{200} = 4$ . This is

due to the lack of good constraints on the shear profile near the center so only the total mass  $M_{200}$  is a reliable measure. These weak lensing masses were compared to the X-ray masses derived from *XMM-Newton* data. Over the 11 clusters, we find a good match between these two mass estimators for 7 clusters while we found 4 outliers, thus having almost a  $1\sigma$  agreement in the two methods. Such results are consistent with other similar studies performed for lower redshift samples.

The primary goal of this study was to look for correlations between the total mass of galaxy clusters and several baryonic tracers. In our sample of massive clusters, we found that the total mass is proportional to the optical richness of galaxies. This result is in good agreement with previous works at lower redshifts (Becker et al. 2007; Johnston et al. 2007; Reyes et al. 2008; Rykoff et al. 2008; Mandelbaum et al. 2008; Rozo et al. 2009). We reach the same conclusion for the correlation between mass and optical luminosity, with a constant ratio  $M/L$ , even if the correlation is weaker with a larger intrinsic dispersion. Using XMM-Newton data and the weak lensing masses, we build scaling relations with the X-ray total luminosity and the global spectroscopic temperature. Both correlations, although weakly constrained due to limited coverage of the mass range, give results in good agreement with previous studies: (i) the mass-luminosity relation presents a non self-similar slope, larger than expected from a purely gravitational model of structure formation. (ii) the mass-temperature relation is roughly compatible with the hierarchical prediction. We have extended our investigation of the  $L_X - M$  relation by combining our cluster sample with two samples of groups and clusters for which weak lensing masses were obtained (Rykoff et al. 2008; Leauthaud et al. 2010). The resulting  $L_X - M_{200}$  relation covers nearly two decades in mass and displays a regular shape with a well constrained slope.

Even if the limited size of our sample and its reduced mass range coverage allow us to only probe the high end of the mass distribution of clusters, we have demonstrated the synergy with the X-ray measurements (i.e., mass, luminosity and temperature). More specifically, we have confirmed that the scaling relations with the lensing mass proxy are already in place at  $z \sim 0.5$ , with, at first order, no significant departures from the same relations at lower redshift (assuming a self-similar evolution). The limited quality of the lensing data for our sample restricts the added value of a joint analysis, but the weak lensing and X-ray coverage of cluster prove to be complementary. Indeed X-ray data allow, to efficiently probe the central regions out to about  $R_{500}$ . Beyond this radius the X-ray brightness rapidly drops, whereas the weak-lensing signal picks up to characterize the outer parts of massive halos. A perspective work would be to investigate the strong lensing signal (see Table 1) of each cluster in our sample, in order to perform a full lensing analysis from the inner part (with the strong lensing signal) to the outer parts (with the weak lensing signal). This would provide a coherent mass proxy estimator to be compared directly with X-ray and dynamical proxies.

Finally, in the perspective of large optical surveys such as the Euclid space mission, self calibrated mass proxies will be needed for the full scientific exploitation of the mission. The  $M - N$  is an obvious candidate, which tight calibration will require validation against other relations and mass proxies, such as the X-ray mass. The  $M - N$  relation we provide in this paper is an early result in the redshift range  $0.4 < z < 0.6$ . It illustrates the difficulty to constrain this particular scaling relation. Provided the  $N$  estimator is made as universal as possible, which can be a non trivial task, this relation is promising in the framework of optical surveys.

*Acknowledgements.* We wish to thank Roser Pello for many fruitful discussions. She provided the catalogs of photometric redshifts built from the CFHTLS Deep fields which are used in this work. We are grateful to the TERAPIX team who processed part of the data efficiently. We also thank the Programme National de Cosmologie et Galaxies of the CNRS for financial support. ML acknowledges the Centre National de la Recherche Scientifique (CNRS) for its support. The Dark Cosmology Centre is funded by the Danish National Research Foundation. The present work is based on observations obtained with XMM-Newton an ESA science mission with instruments and contributions directly funded by ESA

Member States and the USA (NASA). This research used the facilities of the Canadian Astronomy Data Centre operated by the National Research Council of Canada with the support of the Canadian Space Agency. This work is based on observations obtained with MegaPrime/MegaCam, a joint project of CFHT and CEA/DAPNIA, at the Canada-France-Hawaii Telescope (CFHT) which is operated by the National Research Council (NRC) of Canada, the Institut National des Sciences de l'Univers of the Centre National de la Recherche Scientifique (CNRS) of France, and the University of Hawaii.

## References

- Akritis, M. G. & Bershad, M. A. 1996, *Astrophys. J.*, 470, 706  
 Albrecht, A., Bernstein, G., Cahn, R., et al. 2006, *ArXiv Astrophysics e-prints*  
 Allen, S. W. 1998, *Mon. Not. R. Astron. Soc.*, 296, 392  
 Andreon, S. & Hurn, M. A. 2010, *Mon. Not. R. Astron. Soc.*, 404, 1922  
 Arnaud, M., Aghanim, N., & Neumann, D. M. 2002, *Astron. & Astrophys.*, 389, 1  
 Arnaud, M., Pratt, G. W., Piffaretti, R., et al. 2010, *Astron. & Astrophys.*, 517, A92  
 Bahcall, N. A. & Cen, R. 1992, *Astrophys. J.*, 398, L81  
 Bardeau, S., Kneib, J.-P., Czoske, O., et al. 2005, *Astron. & Astrophys.*, 434, 433  
 Bardeau, S., Soucail, G., Kneib, J.-P., et al. 2007, *Astron. & Astrophys.*, 470, 449  
 Bartelmann, M. & Schneider, P. 2001, *Physics Reports*, 340, 291  
 Becker, M. R., McKay, T. A., Koester, B., et al. 2007, *Astrophys. J.*, 669, 905  
 Böhringer, H., Schuecker, P., Pratt, G. W., et al. 2007, *Astron. & Astrophys.*, 469, 363  
 Bolzonella, M., Miralles, J.-M., & Pelló, R. 2000, *Astron. & Astrophys.*, 363, 476  
 Bonnet, H. & Mellier, Y. 1995, *Astron. & Astrophys.*, 303, 331  
 Borgani, S. 2008, in *Lecture Notes in Physics*, Berlin Springer Verlag, Vol. 740, A Pan-Chromatic View of Clusters of Galaxies and the Large-Scale Structure, ed. M. Plionis, O. López-Cruz, & D. Hughes, 287  
 Borgani, S., Murante, G., Springel, V., et al. 2004, *Mon. Not. R. Astron. Soc.*, 348, 1078  
 Bradač, M., Schneider, P., Lombardi, M., & Erben, T. 2005, *Astron. & Astrophys.*, 437, 39  
 Brainerd, T. G., Blandford, R. D., & Smail, I. 1996, *Astrophys. J.*, 466, 623  
 Bridle, S., Gull, S., Bardeau, S., & Kneib, J.-P. 2002, in *Proceedings of the Yale Cosmology Workshop: "The Shapes of Galaxies and their Dark Halos"*, ed. N. P. (World Scientific)  
 Buote, D. A., Gastaldello, F., Humphrey, P. J., et al. 2007, *Astrophys. J.*, 664, 123  
 Croston, J. H., Arnaud, M., Pointecouteau, E., & Pratt, G. W. 2006, *Astron. & Astrophys.*, 459, 1007  
 Croston, J. H., Pratt, G. W., Böhringer, H., et al. 2008, *Astron. & Astrophys.*, 487, 431  
 Cypriano, E. S., Sodr , Jr., L., Kneib, J., & Campusano, L. E. 2004, *Astrophys. J.*, 613, 95  
 Dietrich, J. P., Böhner, A., Lombardi, M., Hilbert, S., & Hartlap, J. 2011, *ArXiv e-prints*  
 Foëx, G., Soucail, G., Pointecouteau, E., Arnaud, M., & Limousin, M. 2012, *Astron. & Astrophys.* to be submitted  
 Gavazzi, R. & Soucail, G. 2007, *Astron. & Astrophys.*, 462, 459  
 Haiman, Z., Mohr, J. J., & Holder, G. P. 2001, *Astrophys. J.*, 553, 545  
 Heymans, C., Van Waerbeke, L., Bacon, D., et al. 2006, *Mon. Not. R. Astron. Soc.*, 368, 1323  
 Hoekstra, H. 2001, *Astron. & Astrophys.*, 370, 743  
 Hoekstra, H. 2003, *Mon. Not. R. Astron. Soc.*, 339, 1155  
 Hoekstra, H. 2007, *Mon. Not. R. Astron. Soc.*, 379, 317  
 Hoekstra, H., Franx, M., & Kuijken, K. 2000, *Astrophys. J.*, 532, 88  
 Ilbert, O., Tresse, L., Zucca, E., et al. 2005, *Astron. & Astrophys.*, 439, 863  
 Johnston, D. E., Sheldon, E. S., Wechsler, R. H., et al. 2007, *ArXiv e-prints*  
 Kaiser, N. 1986, *Mon. Not. R. Astron. Soc.*, 222, 323  
 Kay, S. T. 2004, *Mon. Not. R. Astron. Soc.*, 347, L13  
 Kneib, J., Hudelot, P., Ellis, R. S., et al. 2003, *Astrophys. J.*, 598, 804  
 Kravtsov, A. V., Berlind, A. A., Wechsler, R. H., et al. 2004, *Astrophys. J.*, 609, 35  
 Kravtsov, A. V., Vikhlinin, A., & Nagai, D. 2006, *Astrophys. J.*, 650, 128  
 Lau, E. T., Kravtsov, A. V., & Nagai, D. 2009, *Astrophys. J.*, 705, 1129  
 Le Fèvre, O., Vettolani, G., Garilli, B., et al. 2005, *Astron. & Astrophys.*, 439, 845  
 Leauthaud, A., Finoguenov, A., Kneib, J., et al. 2010, *Astrophys. J.*, 709, 97  
 Limousin, M., Cabanac, R., Gavazzi, R., et al. 2009, *Astron. & Astrophys.*, 502, 445  
 Limousin, M., Kneib, J. P., Bardeau, S., et al. 2007a, *Astron. & Astrophys.*, 461, 881

- Limousin, M., Richard, J., Jullo, E., et al. 2007b, *Astrophys. J.*, 668, 643
- Lin, Y., Mohr, J. J., & Stanford, S. A. 2004, *Astrophys. J.*, 610, 745
- Mahdavi, A., Hoekstra, H., Babul, A., & Henry, J. P. 2008, *Mon. Not. R. Astron. Soc.*, 384, 1567
- Mahdavi, A., Hoekstra, H., Babul, A., et al. 2007, *Astrophys. J.*, 664, 162
- Mandelbaum, R. & Seljak, U. 2007, *J. Cosmology Astropart. Phys.*, 6, 24
- Mandelbaum, R., Seljak, U., Baldauf, T., & Smith, R. E. 2010, *Mon. Not. R. Astron. Soc.*, 405, 2078
- Mandelbaum, R., Seljak, U., Hirata, C. M., et al. 2008, *Mon. Not. R. Astron. Soc.*, 386, 781
- Marinoni, C. & Hudson, M. J. 2002, *Astrophys. J.*, 569, 101
- Markevitch, M. 1998, *Astrophys. J.*, 504, 27
- Maughan, B. J. 2007, *Astrophys. J.*, 668, 772
- Meneghetti, M., Rasia, E., Merten, J., et al. 2010, *Astron. & Astrophys.*, 514, A93+
- Merten, J., Cacciato, M., Meneghetti, M., Mignone, C., & Bartelmann, M. 2009, *Astron. & Astrophys.*, 500, 681
- Metzler, C. A., White, M., & Loken, C. 2001, *Astrophys. J.*, 547, 560
- Morandi, A., Etori, S., & Moscardini, L. 2007, *Mon. Not. R. Astron. Soc.*, 379, 518
- Morandi, A., Pedersen, K., & Limousin, M. 2010, *Astrophys. J.*, 713, 491
- Nagai, D., Vikhlinin, A., & Kravtsov, A. V. 2007, *Astrophys. J.*, 655, 98
- Navarro, J. F., Frenk, C. S., & White, S. D. M. 1995, *Mon. Not. R. Astron. Soc.*, 275, 720
- Navarro, J. F., Frenk, C. S., & White, S. D. M. 1997, *Astrophys. J.*, 490, 493
- Navarro, J. F., Hayashi, E., Power, C., et al. 2004, *Mon. Not. R. Astron. Soc.*, 349, 1039
- Oguri, M., Bayliss, M. B., Dahle, H., et al. 2011, ArXiv e-prints
- Oguri, M., Hennawi, J. F., Gladders, M. D., et al. 2009, *Astrophys. J.*, 699, 1038
- Okabe, N., Takada, M., Umetsu, K., Futamase, T., & Smith, G. P. 2010a, *Publ. Astron. Soc. Japan*, 62, 811
- Okabe, N. & Umetsu, K. 2008, *Publ. Astron. Soc. Japan*, 60, 345
- Okabe, N., Zhang, Y., Finoguenov, A., et al. 2010b, *Astrophys. J.*, 721, 875
- Pointecouteau, E., Arnaud, M., & Pratt, G. W. 2005, *A&A*, 435, 1
- Popesso, P., Biviano, A., Böhringer, H., Romaniello, M., & Voges, W. 2005, *Astron. & Astrophys.*, 433, 431
- Pratt, G. W., Arnaud, M., Piffaretti, R., et al. 2010, *Astron. & Astrophys.*, 511, A85+
- Pratt, G. W., Böhringer, H., Croston, J. H., et al. 2007, *A&A*, 461, 71
- Pratt, G. W., Croston, J. H., Arnaud, M., & Böhringer, H. 2009, *A&A*, 498, 361
- Radovich, M., Puddu, E., Romano, A., Grado, A., & Getman, F. 2008, *Astron. & Astrophys.*, 487, 55
- Reiprich, T. H. & Böhringer, H. 2002, *Astrophys. J.*, 567, 716
- Reyes, R., Mandelbaum, R., Hirata, C., Bahcall, N., & Seljak, U. 2008, *Mon. Not. R. Astron. Soc.*, 390, 1157
- Rozo, E., Rykoff, E. S., Evrard, A., et al. 2009, *Astrophys. J.*, 699, 768
- Rykoff, E. S., Evrard, A. E., McKay, T. A., et al. 2008, *Mon. Not. R. Astron. Soc.*, 387, L28
- Seitz, C. & Schneider, P. 1997, *Astron. & Astrophys.*, 318, 687
- Skibba, R. A., van den Bosch, F. C., Yang, X., et al. 2011, *Mon. Not. R. Astron. Soc.*, 410, 417
- Tyson, J. A. & Seitzer, P. 1988, *Astrophys. J.*, 335, 552
- Vikhlinin, A., Kravtsov, A., Forman, W., et al. 2006, *Astrophys. J.*, 640, 691
- Vikhlinin, A., Kravtsov, A. V., Burenin, R. A., et al. 2009, *Astrophys. J.*, 692, 1060
- Voit, G. M. 2005, *Reviews of Modern Physics*, 77, 207
- Voit, G. M., Bryan, G. L., Balogh, M. L., & Bower, R. G. 2002, *Astrophys. J.*, 576, 601
- Wang, S., Khoury, J., Haiman, Z., & May, M. 2004, *Phys. Rev. D*, 70, 123008
- Weiner, B. J., Phillips, A. C., Faber, S. M., et al. 2005, *Astrophys. J.*, 620, 595
- White, S. D. M., Navarro, J. F., Evrard, A. E., & Frenk, C. S. 1993, *Nature*, 366, 429
- Zhang, Y., Finoguenov, A., Böhringer, H., et al. 2008, *Astron. & Astrophys.*, 482, 451
- Zhang, Y., Okabe, N., Finoguenov, A., et al. 2010, *Astrophys. J.*, 711, 1033

Annexes

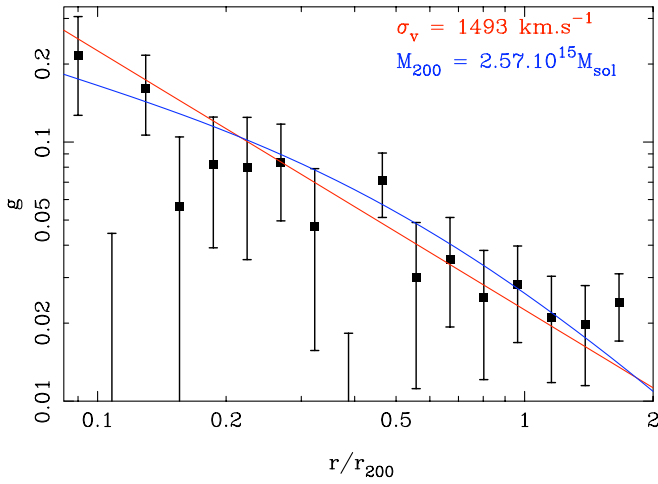


**Fig. 10.** Reduced shear profile normalized by the virial radius  $g(r/R_{200})$  for the galaxy cluster MS 0015.9+1609. The velocity dispersion  $\sigma_v$  and the total mass  $M_{200}$  fitted to this profile are given (red curve for the SIS model, blue one for the NFW model).

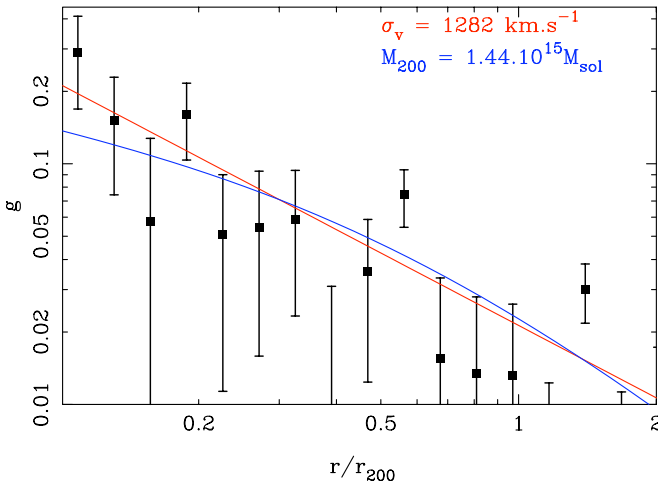


**Fig. 11.** Same as Figure 10 for the cluster MS 0451.6-0305.

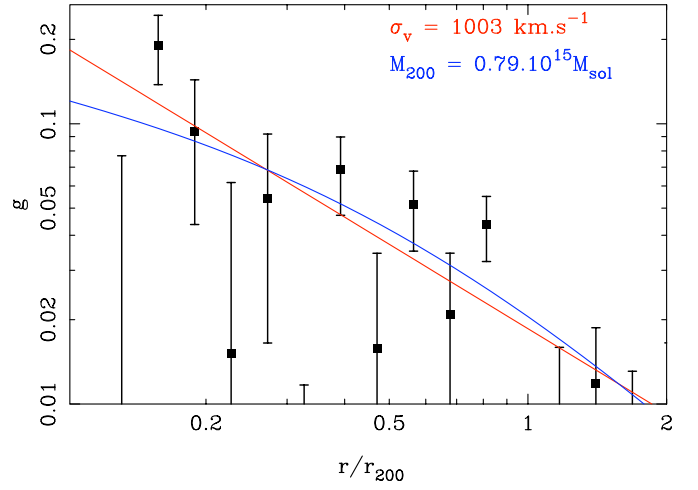


**Fig. 12.** Same as Figure 10 for the cluster RXC J0856.1+3756.

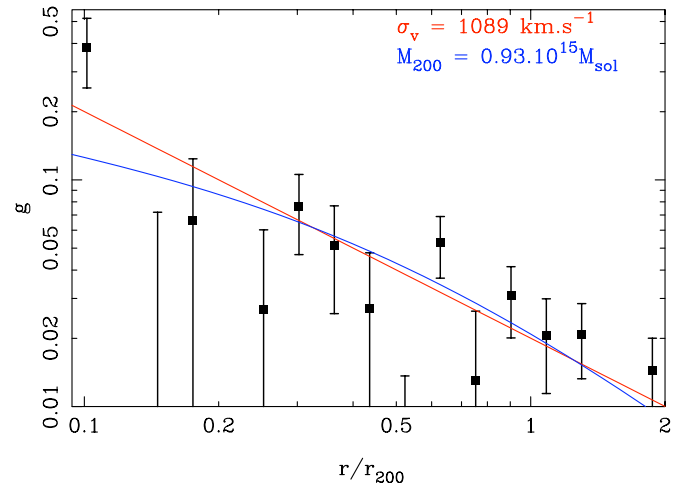


**Fig. 13.** Same as Figure 10 for the cluster RX J0943.0+4659.

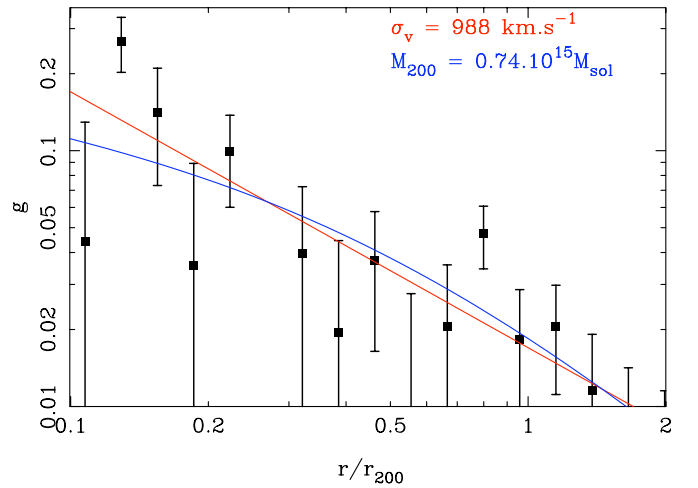


**Fig. 14.** Same as Figure 10 for the cluster RXC J1003.0+3254.

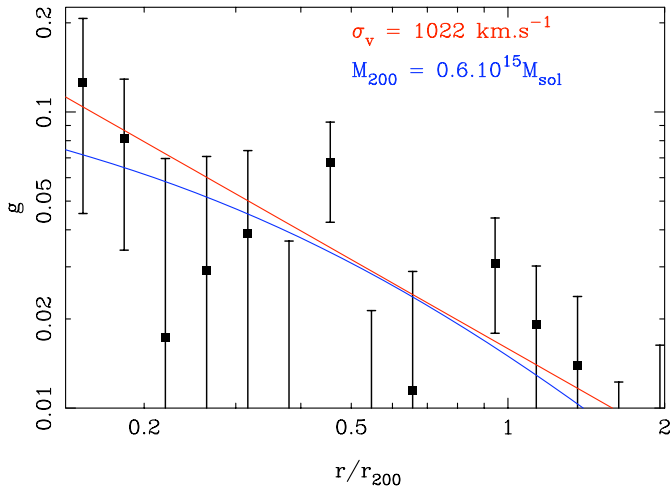


**Fig. 15.** Same as Figure 10 for the cluster RX J1120.1+4318.

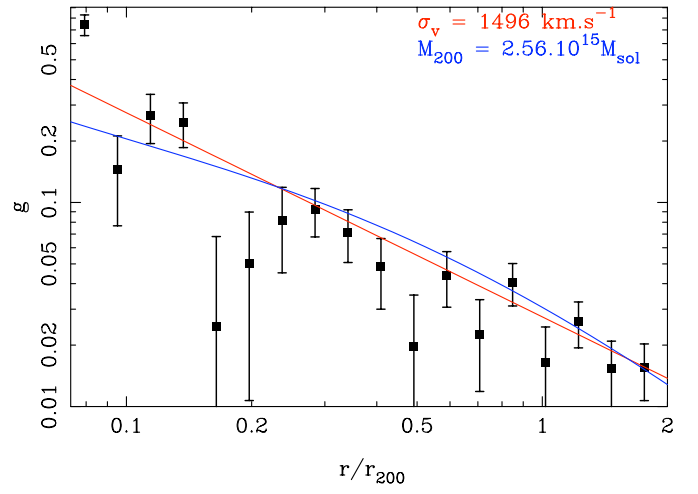


**Fig. 18.** Same as Figure 10 for the cluster RX J1347.5-1144.

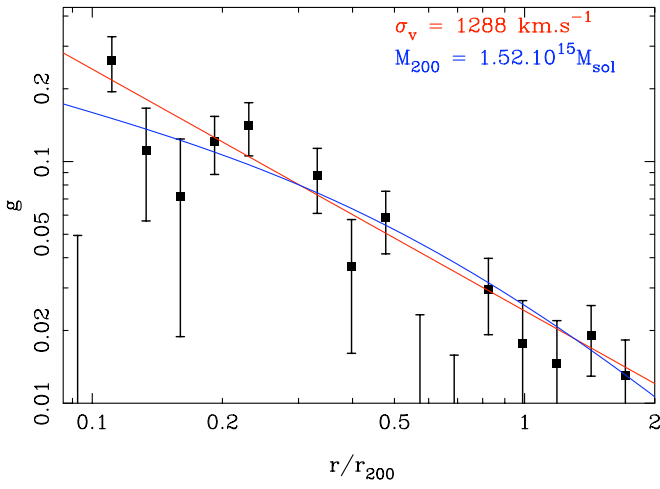


**Fig. 16.** Same as Figure 10 for the cluster RXC J1206.2-0848.

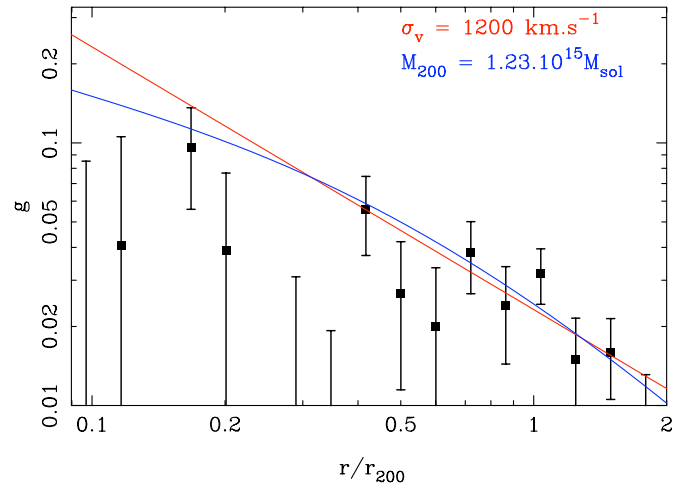


**Fig. 19.** Same as Figure 10 for the cluster MS 1621.5+2640.

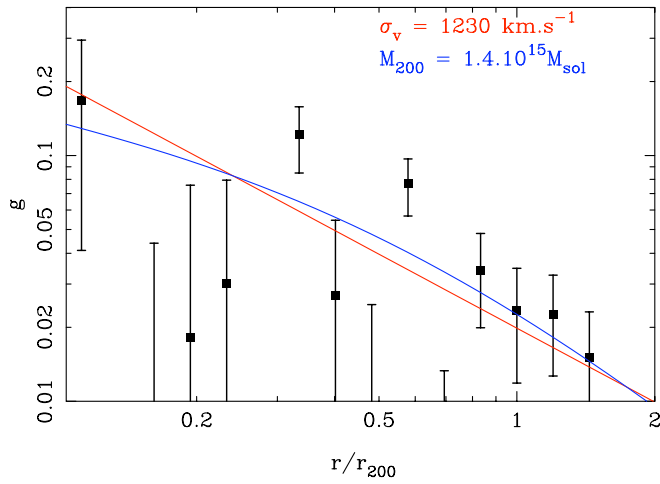


**Fig. 17.** Same as Figure 10 for the cluster MS 1241.5+1710.

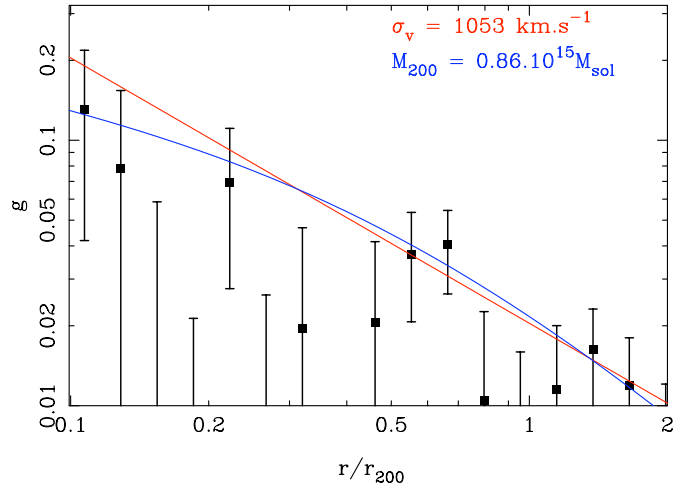


**Fig. 20.** Same as Figure 10 for the cluster RX J2228.5+2036.